Preprint Title The Au/$CuNiCoS_4$/*p*-Si photodiode: electrical and morphological characterization

Authors Adem KOCYIGIT, Adem SARILMAZ, Teoman ÖZTÜRK, Faruk OZEL and Murat YILDIRIM

Publication Date 19 Apr. 2021

Article Type Full Research Paper

ORCID® iDs Adem KOCYIGIT - https://orcid.org/0000-0002-8502-2860; Murat YILDIRIM - https://orcid.org/0000-0002-4541-3752

The Au/$CuNiCoS_4$/*p*-Si photodiode: electrical and morphological characterization

Adem Koçyiğit[1,2], Adem Sarılmaz[3], Teoman Öztürk[4], Faruk Ozel[3,5**], Murat Yıldırım[6*]

[1]Department of Electrical Electronic Engineering, Engineering Faculty, Igdir University, 76000 Igdir, Turkey

[2]Department of Electronics and Automation, Vocational High School, Bilecik Şeyh Edebali University, 11230, Bilecik, Turkey

[3]Department of Metallurgical and Materials Engineering, Faculty of Engineering, Karamanoğlu Mehmetbey University, 70200, Karaman, Turkey

[4]Department of Physics, Faculty of Science, Selcuk University, 42130, Konya, Turkey

[5]Scientific and Technological Research and Application Center, Karamanoglu Mehmetbey University, 70200, Karaman, Turkey

[6]Department of Biotechnology, Faculty of Science, Selcuk University, 42130, Konya, Turkey

Corresponding Authors:

* muratyildirim@selcuk.edu.tr (Murat Yıldırım)

** farukozell@gmail.com (Faruk Ozel)

Abstract

In this present work, the CuNiCoS4 thiospinel nanocrystals were synthesized by hot-injection method and characterized by x-ray diffractometer (XRD) and high resolution transmission electron microscope HR-TEM as well as scanning electron microscope (SEM) with energy dispersive spectroscopy (EDS) detector. The XRD, EDS and HR-TEM analysis confirmed the composition of the CuNiCoS4 and successfully synthesis. The obtained CuNiCoS4 thiospinel nanocrystals were tested for photodiode as well as capacitance applications between the Au and p-type Si by *I-V* and *C-V* characteristics. The fabricated Au/CuNiCoS4/p-Si device exhibited good rectifying property as well as high photoresponse activity and low series resistance and high shunt resistance. The *C-V* characteristics revealed that the obtained photodiode has voltage and frequency dependent capacitance and conductance characteristics. The fabricated device with CuNiCoS4 thiospinel nanocrystals can be employed and developed for high efficiency optoelectronic applications.

Keywords

CuNiCoS4; Schottky devices; Au/CuNiCoS4/p-Si device; optoelectronic applications

Introduction

Recently, spinel materials have attracted great attention due their unique electronic, magnetic, and optical and gas sensing properties. Because of these properties, spinel materials can be employed in the data storage applications, lithium ion batteries, gas sensors and medical diagnostics [1,2]. The spinels have a cubic crystal form and their general chemical formula is AB_2X_4. In this formula, A and B are cations which can be

divalent, trivalent or tetravalent and X represents anions of chalcogen, oxygen or sulfur [3]. Among the spinel material groups, thiospinels are one of the most interesting spinels and are obtained by adopting sulfide into their structure [4,5]. These sulfur based spinel compounds have high potential to be used in energy applications due to their remarkable crystal, electric, thermoelectric, magnetic, and optical properties [6,7]. There are many studies in the literature on the usage of thiospinels in batteries, super-capacitors and electrochemical reactions applications [8–12]. However, there are only two studies on the synthesis and application of quaternary $CuNiCoS_4$ nanocrystals. The former study is the synthesis of the $CuNiCoS_4$ thiospinels which was reported by Thompson [13]. The latter is another study on the synthesis and photocatalytic hydrogen evolution which was performed by our working group [8]. According to this study, the optical characterization results of the $CuNiCoS_4$ nanocrystals have revealed that the band gap value is in good agreement for optoelectronic devices. To the best of our knowledge, there is no study on electrical properties of $CuNiCoS_4$ based photodiodes.

The usage of various materials between the metal-semiconductor devices as interfacial layers is hot topic in the research and development of more efficient metal semiconductor devices such as photodiodes, photodetectors and transistors [14–16]. This interfacial layer provides to control the current flow between the metal and semiconductor as well as give more carriers to the device under the illumination [17,18]. The thiospinel $CuNiCoS_4$ nanocrystals can be inserted between the metal and semiconductor as interfacial layer to increase the effect of the illumination and to control electrical properties of the metal-semiconductor devices.

In this study, we synthesized $CuNiCoS_4$ thiospinel nanocrystals via hot-injection method and employed them to interfacial layer between the Au metal and *p*-Si by spin coating technique in order to fabricate Au/$CuNiCoS_4$/*p*-Si photodiodes. The XRD, HR-

TEM and SEM analyses were employed to characterize the thiospinel $CuNiCoS_4$ nanocrystals, and The *I-V* and *C-V* measurements were performed to determine the photodiode and capacitive behaviors of the Au/$CuNiCoS_4$/*p*-Si devices.

Experimental Details

Materials

Copper(II) acetate ($CuAc_2$), nickel(II) acetate ($NiAc_2$), cobalt acetate ($CoAc_2$), trioctylphosphine oxide (TOPO), 1-dodecanethiol (DDT), tert-Dodecylmercaptan (tert-DDT), 1-octadecene (ODE) and ethanol were purchased from Aldrich. Toluene was bought from VWR.

Synthesis of $CuNiCoS_4$ nanocrystals [8]:

Equal and stoichiometric amounts (0.125 mmol) of $CuAc_2$, $NiAc_2$, $CoAc_2$ and 1.75 mmol TOPO were mixed with 10 ml ODE in a three-neck flask under Ar atmosphere for 30 minutes. Then the reaction solution was placed in a heating mantle, and the temperature was set to 210 °C. Separately, the sulfur solution was prepared by mixing 0.125 ml DDT with 0.875 ml *tert*-DDT in a glass vial, and the solution was heated up to 70 °C. When the reaction temperature reached 120 °C, color of the reaction solution turned to black, and the sulfur solution was added into the reaction medium. The solution was heated until the synthesis temperature reached to 210 °C, and it was stirred for 30 minutes at this temperature. At the end of synthesis time, the three-neck flask was removed from the heating mantle, and the solution was allowed to cool down to 80 °C. Finally, $CuNiCoS_4$ nanocrystals were precipitated via centrifugation by adding 35 ml toluene and 5 ml ethanol.

Fabrication of the Al/$CuNiCoS_4$/p-Si device

A *p*-type Si wafer oriented (100) direction was used as substrate as well as semiconductor material for the Au/$CuNiCoS_4$/*p*-Si photodiode. Firstly, the wafer was cut to 2 cm^2 pieces, and acetone and propanol were used to clean the pieces in an ultrasonic cleaner. Then, they were immersed in HF:H_2O (1:10) solution for eliminating the oxide layer and impurities from the surfaces. In order to obtain ohmic contact, a 100 nm Al layer was evaporated to back surface of the pieces, then annealing process was applied to the pieces for 5 minutes in N_2 atmosphere at 500 °C. The thiospinel $CuNiCoS_4$ nanocrystals were coated on the front surface of the pieces by a spin coater. A 100 nm Au metal layer was covered on the thiospinel $CuNiCoS_4$ nanocrystals film surfaces as rectifying contact. Thus, the Au/$CuNiCoS_4$/*p*-Si device was completed as photodiode. The schematic illustration of the fabricated photodiode device has been shown in Fig. 1.

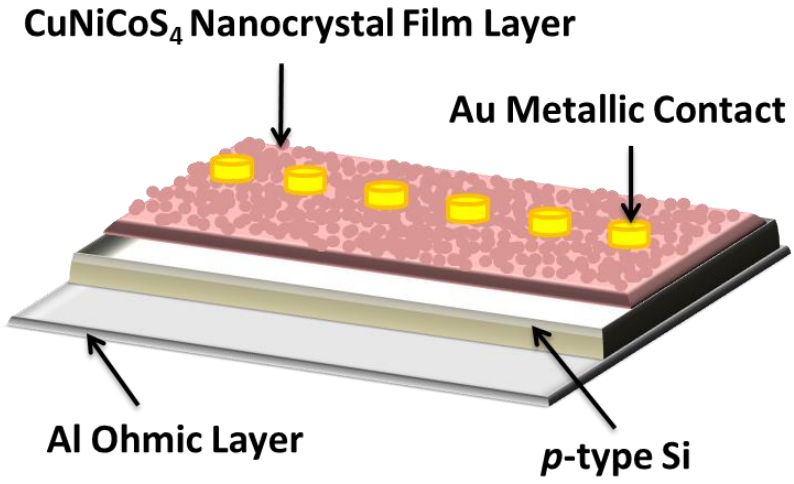

Figure 1. The schematic illustration of the fabricated Au/$CuNiCoS_4$/*p*-Si photodiode

Characterization

A Bruker D8 diffractometer was performed to collect the XRD patterns of the thiospinel $CuNiCoS_4$ nanocrystals in order to investigate their structural properties using Cu-

K_α radiation ($\lambda = 0.15418$ nm). A FEI brand TALOS F200S model tunneling electron microscope (TEM) was used to understand the structural as well as morphological behaviors of the nanocrystals. The Zeiss-Evo SEM-EDX was employed to determine surface morphology and EDS pattern of nanocrystals. *I-V* measurements were obtained by Fytronix FY-7000 under dark and illumination conditions from 20 mW to 100 mW by 20 mW interval. The wavelength of the used light source was in the range of 400–1100 nm. *C-V* measurements were collected by Keithley 4200 SCS.

Results and Discussion

Structural characterization

The crystal structure, phase and purity of produced nanocrystals were investigated by XRD analysis, and the XRD pattern of the nanocrystals has been shown in Fig. 2a. When the XRD pattern is examined in detail, it is seen that the diffraction peaks match with cubic phase of Fd-3m (227) space group. Furthermore, main diffraction peaks at 26.5, 31.1, 38.1, 46.0, 50.0 and 54.7 degrees correspond to the planes of (022), (113), (004), (224), (115) and (044), respectively (JCPDS 00-042-1450). Moreover, because of the performed analyzes, the XRD peaks of the other phases have not been detected, and this result confirms synthesized nanocrystals have pure crystal structure.

TEM images of the $CuNiCoS_4$ nanocrystals have been indicated in Fig. 2b. As can be seen from TEM results, agglomerated spherical shaped nanocrystals were formed due to magnetic effect and electrostatic-steric-electrosteric forces [19]. Furthermore, due to the performed calculations, the average particle sizes of the $CuNiCoS_4$ nanocrystals were determined as 6.5±1 nm.

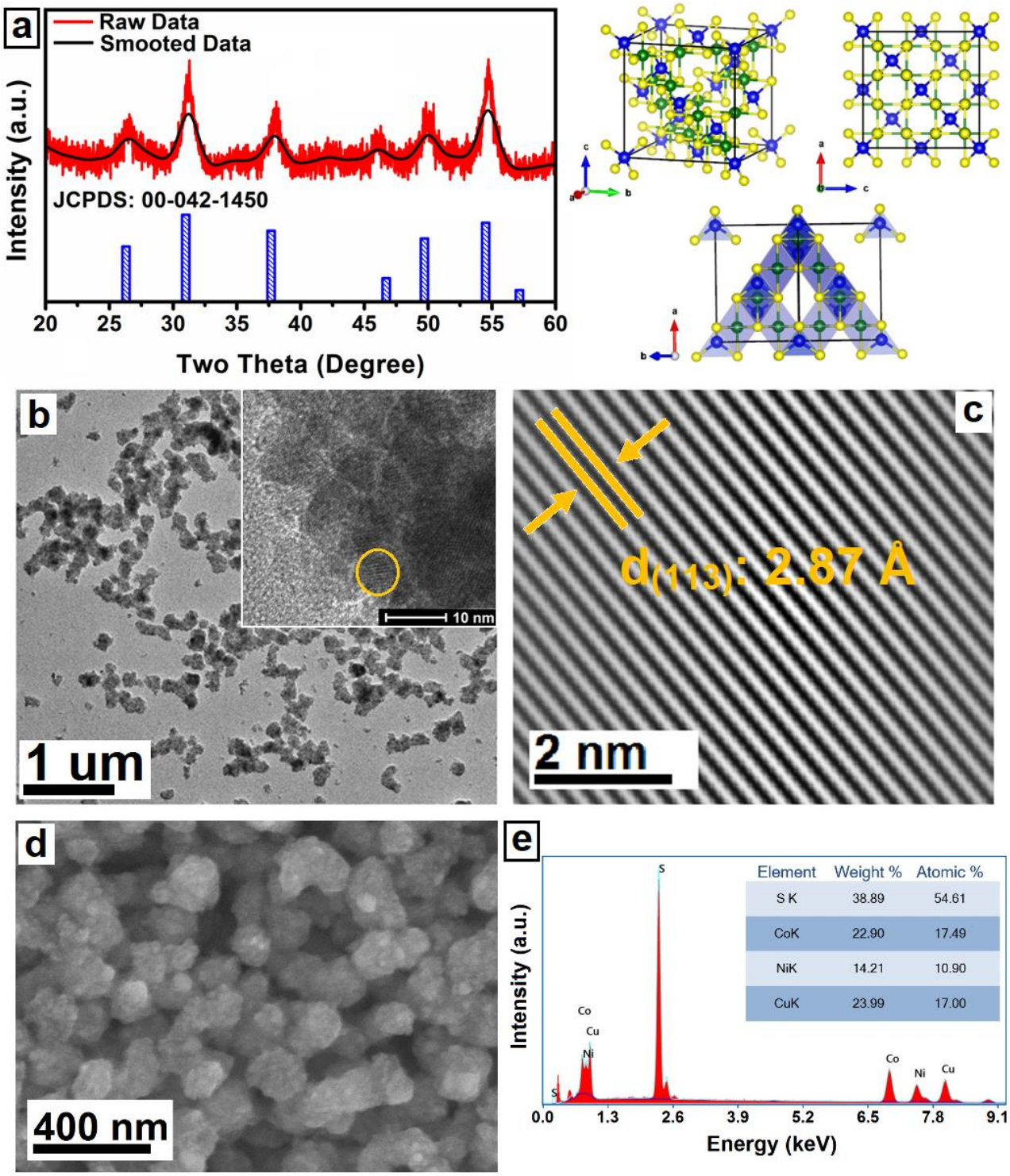

Figure 2. (a) XRD pattern and crystal structure modeling, **(b)** TEM image, **(c)** HR-TEM interplanar spacing image, **(d)** FE-SEM image and **(e)** EDS pattern of the $CuNiCoS_4$ nanocrystals

The interplanar spacing was detected from the HR-TEM image given in Fig. 2c, and the d value was calculated as 2.87 Å corresponding to (113) plane of the cubic crystal structure. Fig. 2d shows FE-SEM images of nanocrystals. The obtained nanocrystals have agglomerated morphology compatible with TEM results. The surface of the $CuNiCoS_4$ nanocrystal layers is smooth and free from pinholes. Components and stoichiometric rates of the $CuNiCoS_4$ nanocrystals were analyzed with the EDS characterization method, and these results were given in Fig. 2e. The chemical composition of the nanocrystals was determined as $Cu_{1.24}(NiCo)_{2.08}S_4$, and these ratios quite close to theoretical composition ($CuCo_2S_4$). The morphological characterization results of the $CuNiCoS_4$ nanocrystals have confirmed that the nanocrystals are suitable for interfacial layers of the photodiodes.

Optical Properties

The optical properties of $CuNiCoS_4$ nanocrystals were investigated by absorbance and diffuse reflectance spectroscopies given in Fig. 3. As can be seen in Fig. 3a, synthesized nanocrystals have strong absorption in a broad spectrum including the ultra-violet and the near-infrared region. Furthermore, the graph of diffuse reflectance spectroscopy performed was given as an inset plot in Fig. 3a. The obtained result show that the absorption of $CuNiCoS_4$ nanocrystals increases from 1200 nm to 300 nm which is compatible with the absorbance result.

The optical band gap of thiospinel $CuNiCoS_4$ was calculated from Tauc and Kubelka-Munk Equations. $(F(R_\infty)h\nu)^2$-Photon Energy graph was plotted to estimate the band gap of nanocrystals with direct band transition type [8]. The bandgap was determined as 1.66 eV by extrapolating the linear portion of the band energy graph given in Fig. 3b.

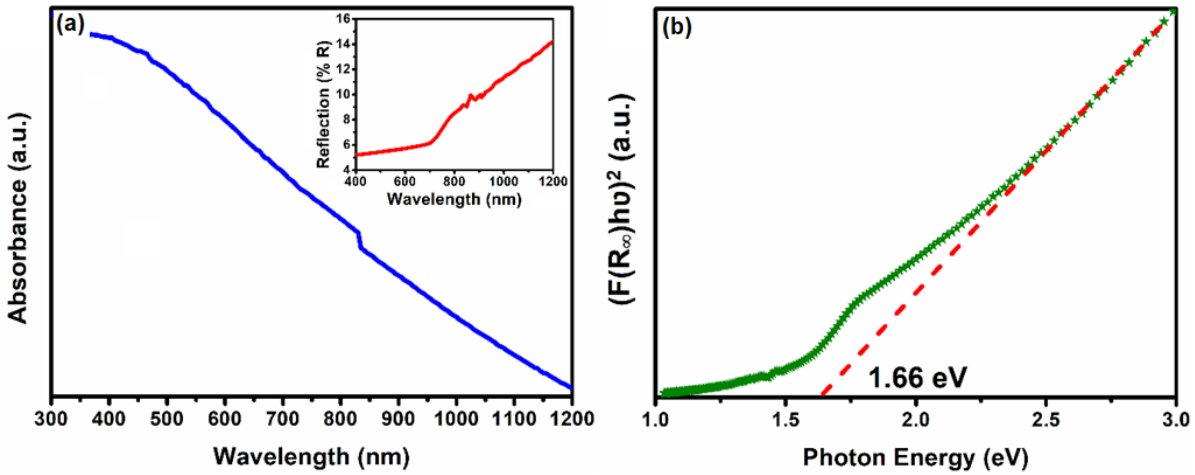

Figure 3. (a) Absorbance spectroscopy graph (inset figure: diffuse reflectance graph) and (**b)** bandgap energy diagram of $CuNiCoS_4$ nanocrystals.

Electrical Properties

In order to determine electrical performance of the Au/$CuNiCoS_4$/*p*-Si, the *I-V* measurements were performed on the photodiode under dark and various illumination conditions. The *I-V* characteristics of the Au/$CuNiCoS_4$/*p*-Si photodiode have been shown in Fig. 4 depending on the light power illumination intensities. The obtained photodiode exhibited normal diode characteristics and good rectifying property. The rectifying ratio (*RR*) values of the photodiode were changed with increasing light power intensity. The *RR* value was calculated as 53.25 under dark, but it was obtained as 35.53×10^3 under 20 mW light power and then decreased to 21.25 with increasing light power. The sharp increase at the *RR* value under 20 mW light power and slowly decrease with increasing light intensity can be attributed to the increasing of the current in the interface at forward biases greatly [20]. The changes of the *RR* values with light power have been displayed in inset of the Fig. 4.

The fabricated Au/$CuNiCoS_4$/*p*-Si photodiode exhibited almost linearly growth at the current values with increasing light power intensity due to enhancing number of charge

carriers in the interface at reverse biases. The photocurrent value was obtained 1000 times higher than the dark current owing to the existence of interfacial $CuNiCoS_4$ layer as well as semiconductor *p*-Si [21,22]. The nearly 1000 times increasing of the current at zero bias voltage from dark to 20 mW/cm^2 light power illumination intensity can be attributed to increasing of the carriers due to illumination in the interface of the Au/$CuNiCoS_4$/*p*-Si device. The naturally composed depletion region between the metal and semiconductor can be able to cause current in the device. Furthermore, the effect of the $CuNiCoS_4$ layer also can be thought this increase of the current at zero bias voltage due its high absorption properties of the solar light. The $CuNiCoS_4$ layer has suitable band gap value for solar spectrum and can be used for optoelectronic applications such as photodiode and photodetector due to good response of the increasing light power illumination intensities [8].

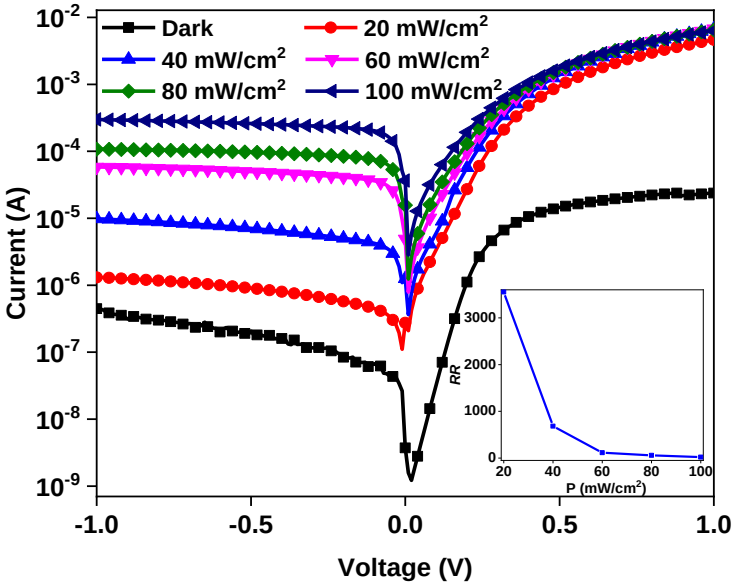

Figure 4. The *I-V* characteristics as well as *RR* changes of the Au/$CuNiCoS_4$/*p*-Si photodiode for various illumination intensities

The diode parameters such as ideality factor (*n*), series resistance (R_s) as well as barrier height (ϕ_b) of the fabricated Au/CuNiCoS$_4$/*p*-Si device provide information to understand electrical characteristics. These parameters can be extracted from the *I-V* measurements by various techniques such as thermionic emission theory and Norde method. The current (*I*) is calculated by next equation from thermionic emission theory:

$$I = I_0 \exp\left(\frac{qV}{nkT}\right)\left[1 - \exp\left(-\frac{qV}{nkT}\right)\right] \quad (1)$$

where I_0 is saturation current and calculated by next formula:

$$I_0 = AA^*T^2 \exp\left(-\frac{q\phi_b}{kT}\right) \quad (2)$$

where k and q show Boltzmann's constant and the charge of the electron. *T*, *A*, and A^* shows the temperature, diode area (in here *A* is equal to 7.85×10^{-3} cm^2) and Richardson constant (32 A cm^{-2} K^{-2} for *p*-type Si), respectively. The Eq. 2 helps to calculate the ϕ_b by the determination of the saturation current value from *I-V* curve of the Au/CuNiCoS$_4$/*p*-Si photodiode. The slope of the second linear region at the *I-V* curve helps to calculate the *n* value for $V \geq 3kT/q$ by following equation:

$$n = \frac{q}{kT}\left(\frac{dV}{d\ln I}\right) \quad (3)$$

and ϕ_b is obtained from the next equation:

$$\phi_b = \frac{kT}{q}\ln\left(\frac{A^*AT^2}{I_0}\right) \quad (4)$$

Light illumination power intensity profile of the calculated *n* and ϕ_b values for Au/CuNiCoS$_4$/*p*-Si photodiode has been displayed in Fig. 5, and the calculated *n* and ϕ_b values were listed in Table 1 for various light power intensity. While the ideality factor values increased from 1.06 to 1.85, barrier height values decreased from 0.81 eV to 0.57 eV with increasing light illumination power intensity. The *n* value under dark condition was obtained so close to the unity, but increasing light intensity caused to the change at the density distribution of the carriers, and thus ideality factor values

increased [23]. The ideality factor value of the Au/CuNiCoS$_4$/*p*-Si photodiode close to unity can be attributed to homogenous interfacial layer of CuNiCoS$_4$.

The interfacial layer can passivate the dangling bonds and decrease the interface state density. Thus, ideality factor values closes to unity [24]. The decrease at the ϕ_b values with increasing light power can be attributed to that charge carriers with high energy pass easily barrier between the metal and semiconductor or more charge carriers is obtained by increasing light power, and thus diffusion of the charges occurs from the barrier [25].

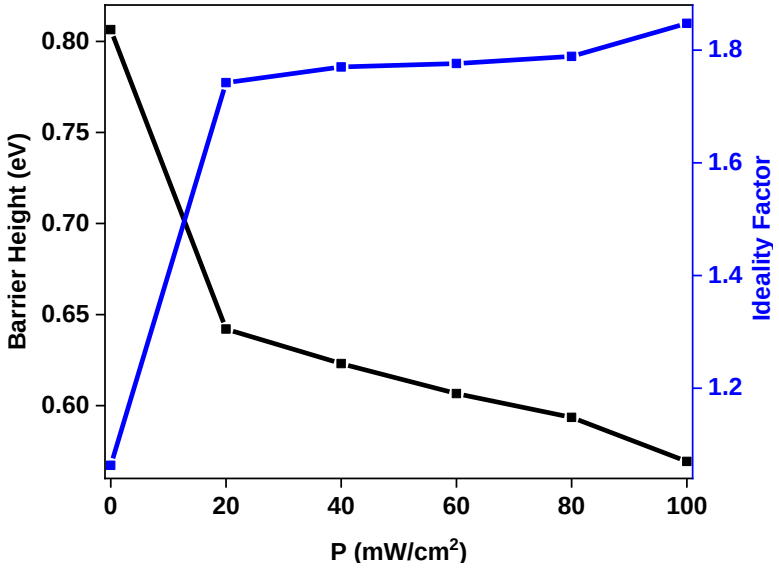

Figure 5. The changing of the *n* and ϕ_b values of the Au/CuNiCoS$_4$/*p*-Si photodiode depending on the light power intensity

The junction resistance (R_j) is another diode parameter to evaluate the fabricated Au/CuNiCoS$_4$/*p*-Si photodiode, and it can be determined from *I-V* characteristics [26]. The R_j contains two component: shunt resistance (R_{sh}) due to contact of metal-semiconductor interface and series resistance (R_s) owing to interfacial layers [27]. The R_j is given by next formula:

$$R_j = \frac{\partial V}{\partial I} \qquad (5)$$

The R_j-V plots of the Au/CuNiCoS$_4$/p-Si photodiode have been indicated in Fig. 6 for various illumination power intensities. While the R_{sh} values are determined from reverse bias R_j values, the R_s values are obtained from the forward biases. The R_{sh} value of the photodiode was obtained 10^7 Ω level, but the R_s value was determined as 10^4 Ω level under dark. The obtained R_s and R_{sh} values have been listed in Table 1 for various illumination intensities. Both the R_s and R_{sh} values decreased with increasing light power intensity. The obtained the R_s and R_{sh} results highlights that the photodiode can be used for optoelectronic application in respect to interfacial layer due to its R_s and R_{sh} level [28]. The slightly increasing of the R_s value of the dark condition can be attributed to constant current with increasing voltage due to the interface states of the device.

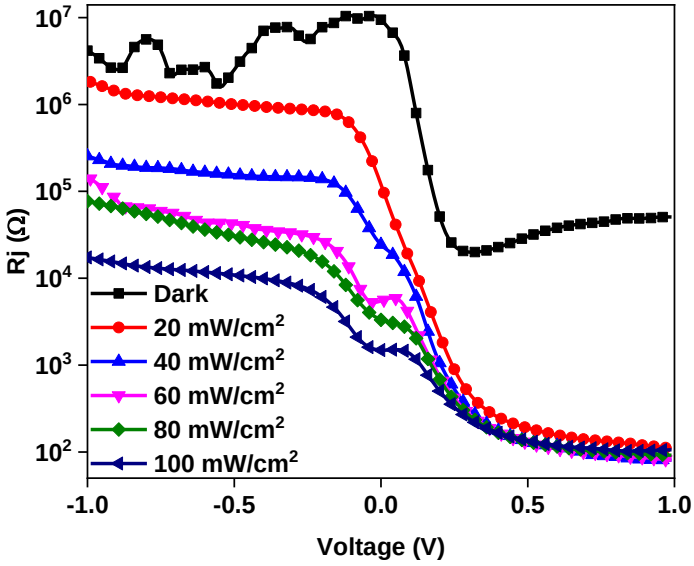

Figure 6. The R_j-V plots of the Au/CuNiCoS$_4$/p-Si photodiode for various light power intensities

Another method to determine the barrier height as well as series resistance value is Norde technique. Norde function is defined by the following formula [29]:

$$F(V) = \frac{V}{\gamma} - \frac{\mathrm{k}T}{\mathrm{q}} ln\left(\frac{I(V)}{AA^*T^2}\right) \qquad (6)$$

where γ is closest integer higher than *n*. *I(V)* is expressed voltage depended current. The ϕ_b and R_s is obtained by next formulas according to Norde technique:

$$\phi_b = F(V_0) + \left[\frac{V_0}{\gamma} - \frac{\mathrm{k}T}{\mathrm{q}}\right] \quad (7)$$

$$R_s = \frac{\gamma - n}{I} \quad \frac{\mathrm{k}T}{\mathrm{q}} \quad (8)$$

where V_0 is the minimum voltage corresponding to *F(V)*. *F(V)* versus *V* plots of the Au/CuNiCoS$_4$/*p*-Si photodiode have been shown in Fig. 7 for various illumination power intensities. The calculated ϕ_b and R_s values are given in Table 1. The *F(V)*-*V* plots exhibited normal Norde function plot, and the *F(V)* values decreased with increasing light power were clearly seen especially low voltage region due to increasing photocurrent. Both the obtained ϕ_b and values R_s are good agreement with the thermionic emission ϕ_b and R_s values. Small differences at the ϕ_b and R_s values can be attributed to approximation technique [27].

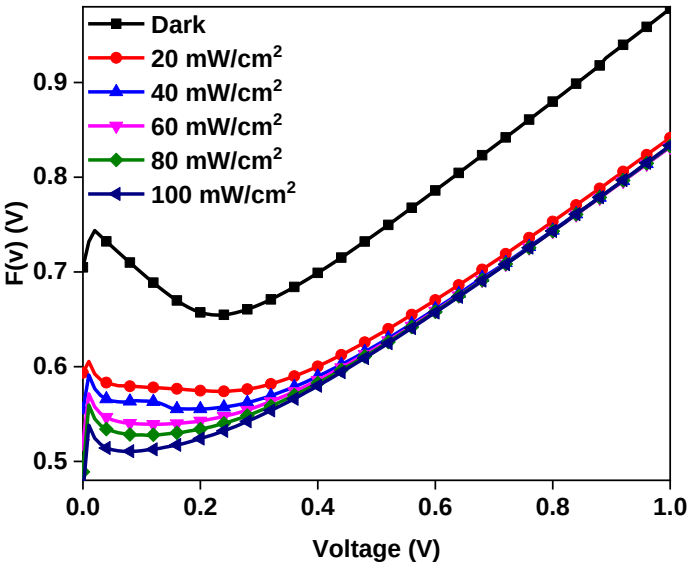

Figure 7. The *F(V)*-*V* plots of the Au/CuNiCoS$_4$/*p*-Si photodiode for various illumination intensities

The responsivity and specific detectivity are other important parameters for a photodiode or photodetector. While the responsivity shows response of the incident

light, the specific detectivity represents the inverse of the noise equivalent power [30]. Both the responsivity and specific detectivity increased with increasing light power and confirmed good performance of the fabricated Au/CuNiCoS$_4$/*p*-Si photodiode.

Table 1. The diode parameters of the Au/CuNiCoS$_4$/*p*-Si photodiode for various methods

Condition	I_0 (A)	n (*I-V*) -	ϕ_b (*I-V*) (eV)	ϕ_bNorde (eV)	R_{sh} (kΩ)	R_s (kΩ)	R_s (Norde) (kΩ)	Responsivity (A/W)	Detectivity (Jones)
Dark	6.58×10^{-10}	1.06	0.81	0.83	7934	19.57	9.12	-	-
20 mW	3.79×10^{-7}	1.74	0.64	0.66	876	0.14	0.13	4.87	9.99×10^{11}
40 mW	7.89×10^{-7}	1.77	0.62	0.62	157	0.13	0.15	6.99	1.39×10^{12}
60 mW	1.49×10^{-6}	1.78	0.61	0.58	33.7	0.14	0.21	13.97	2.68×10^{12}
80 mW	2.47×10^{-6}	1.79	0.59	0.56	22.1	0.14	0.19	12.15	2.33×10^{12}
100 mW	6.29×10^{-6}	1.85	0.57	0.52	7.67	0.13	0.15	10.48	2.11×10^{13}

Log I and photoresponsivity versus *Log P* graphs of the Au/CuNiCoS$_4$/*p*-Si has been indicated in Fig. 8. Both *Log I* and photoresponsivity exhibited increasing profile with increasing light power almost linearly. The linearly increase at the photocurrent with increasing light power intensity can be attributed to photoconductive mechanism of the Au/CuNiCoS$_4$/*p*-Si. According to changes of the photoresponsivity and current with increasing light power, the Au/CuNiCoS$_4$/*p*-Si heterostructure is a promising candidate for optoelectronic applications [31].

The fabricated Au/CuNiCoS$_4$/*p*-Si photodiode was studied with *C-V* and *G-V* measurements depending on the various frequencies to understand frequency response and obtain some other electrical parameters.

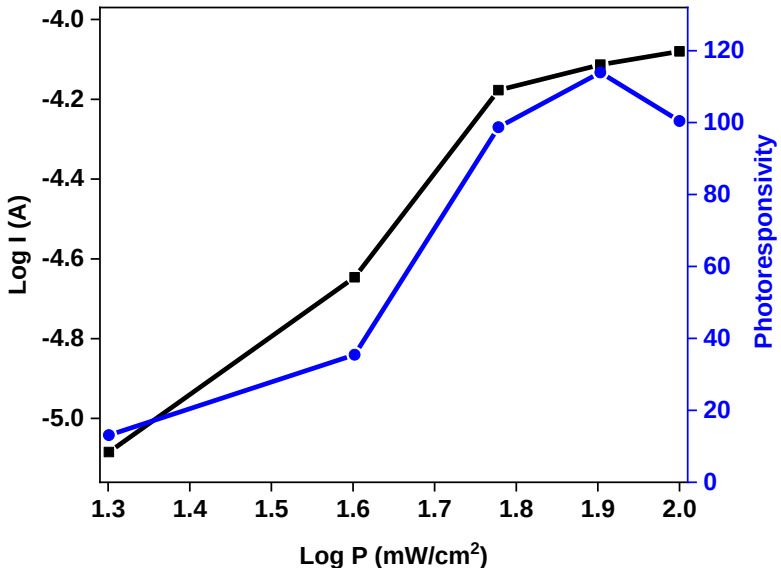

Figure 8. *Log I* and photoresponsivity versus *Log P* of the Au/CuNiCoS$_4$/*p*-Si photodiode for various light illumination intensities

The *C-V* graphs of the Au/CuNiCoS$_4$/*p*-Si photodiode have been exhibited in Fig. 9 for the ranges of 10 kHz to 1 MHz frequency and voltage ±5V. The *C-V* characteristics revealed that the capacitance values did not change in accumulation and depletion regions by changing of the voltage and frequency but increased suddenly in the inversion region and exhibited peaks. The intensity of the peaks decreased towards higher frequency, and the peak positions shifted by changing voltage. The presence of the peaks highlights the existence of the series particular distribution of the interface states or CuNiCoS$_4$ layer [32,33]. The decrease at the capacitance values with increasing frequency can be attributed to that interface states, which caused to capacitance, cannot give response to the high frequency ac signal [34,35].

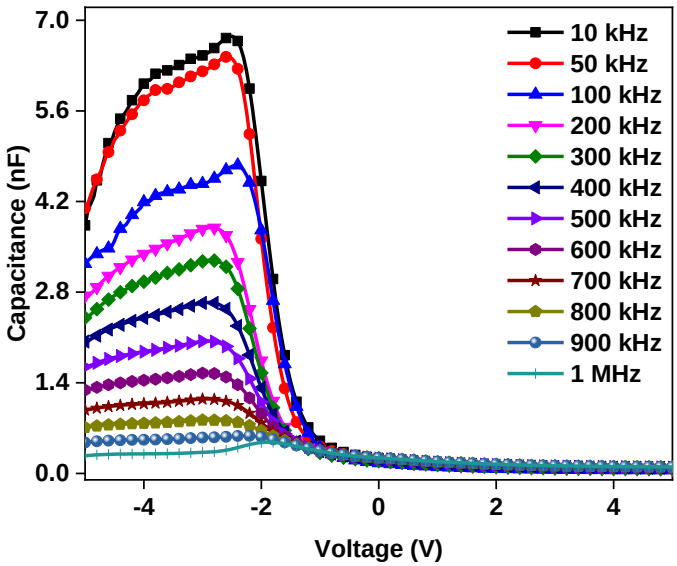

Figure 9. The *C-V* graphs of the Au/CuNiCoS$_4$/*p*-Si photodiode for increasing frequency

The conductance-voltage (*G-V*) graphs of the Au/CuNiCoS$_4$/*p*-Si photodiode have been displayed in Fig. 10 as functions of the frequency and voltage. Again, the conductance values did not change in the accumulation and depletion regions. However, the conductance values affected from the voltage and frequency changes in the inversion region. The conductance values for higher frequency values than 100 kHz increased suddenly and stayed almost constant towards higher inversion region. Furthermore, the conductance values increased with increasing frequency in the inversion region due to effect of the interface states that existence in the photodiode [36,37]. The sudden increase of the conductance values with the increasing reverse bias can be attributed to that applied electric field caused to change of the behavior type of semiconductor.

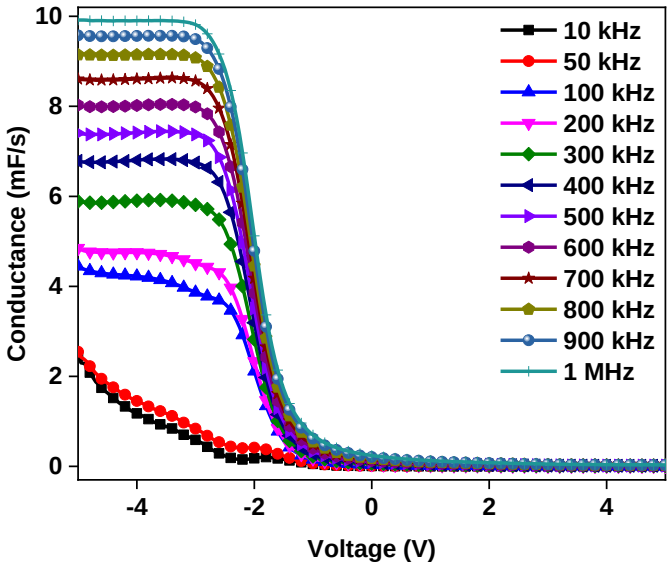

Figure 10. The *G-V* graphs of the Au/CuNiCoS$_4$/*p*-Si photodiode for increasing frequency

The C^{-2}-*V* graphs of the Au/CuNiCoS$_4$/*p*-Si device have been displayed in Fig. 11 for various frequencies. The graphs exhibited sometimes straight lines and sometimes deviation from the linearity due to having non-homogenous interfacial layer of the CuNiCoS$_4$ [38]. Various electrical parameters such as fermi energy level (E_F), barrier height (Φ_b), maximum electric (E_m), depletion width (W_d), doping concentration acceptor atoms (N_a) and interface states (N_{ss}) were calculated from the C^{-2}-*V* graphs and listed in Table 2 for changing frequencies [39].

While the N_a, E_m and Φ_b values usually increased, the E_F, R_s and N_{ss} values decreased by increasing frequency. However, the W_d values increased up to 100 kHz with the increasing frequency, and then decreased towards 1000 kHz. The decreasing of the R_s with increasing frequency can be attributed to increasing of the conductivity of the photodiode. The level of the N_{ss} values for the Au/CuNiCoS$_4$/*p*-Si photodiode is acceptable or proper for a kind of optoelectronic device [40].

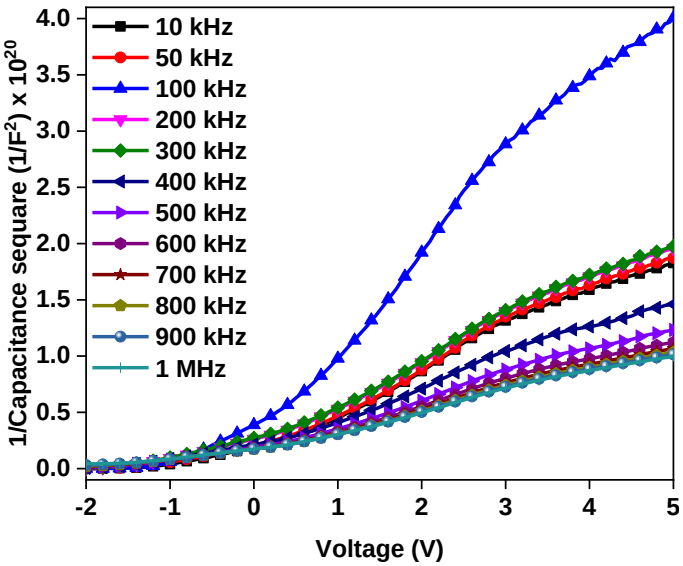

Figure 11. The C^{-2}-V plots of the Au/CuNiCoS$_4$/p-Si photodiode for various frequencies

Table 2. The electrical parameters which were calculated from C^{-2}-V plots of the Au/CuNiCoS$_4$/p-Si photodiode for various frequencies

f (kHz)	N_a (10^{15} cm^{-3})	R_s (Ω)	Φ_b (eV)	E_F (eV)	E_m ($\times10^4$ V/cm)	W_d ($\times10^{-5}$ cm)	N_{ss} ($\times10^{10}$ eV^{-1} cm^{-2})
10	7.822	364.58	1.009	0.138	4.545	3.881	16.693
50	7.605	357.63	1.029	0.138	4.530	3.977	5.140
100	4.670	348.92	1.157	0.151	3.769	5.380	9.702
200	6.972	326.03	1.067	0.141	4.424	4.235	5.576
300	6.823	307.33	1.084	0.141	4.415	4.317	5.357
400	9.034	288.13	1.093	0.134	5.128	3.787	5.295
500	10.181	283.12	1.100	0.131	5.475	3.587	5.353
600	11.058	276.77	1.107	0.129	5.735	3.459	5.446
700	11.522	270.16	1.126	0.128	5.914	3.422	5.570
800	11.805	265.39	1.127	0.127	5.992	3.384	5.719
900	11.877	262.12	1.139	0.127	6.046	3.393	5.912
1000	12.102	264.89	1.154	0.126	6.151	3.388	6.168

The resistance versus voltage (R_i-V) plots of the Au/CuNiCoS$_4$/p-Si photodiode have been given Fig. 12 for changing frequency and voltage. The R_i values usually

decreased with increasing frequency due to increasing conductance values of the Au/CuNiCoS$_4$/*p*-Si photodiode. The frequency depended R_i profiles exhibited peaks in depletion region because of the interface states [41]. The peaks positions shifted towards the inversion region. Furthermore, the R_i values almost did not change in the inversion region but suddenly increased in the depletion region and stayed almost constant same values in the accumulation region.

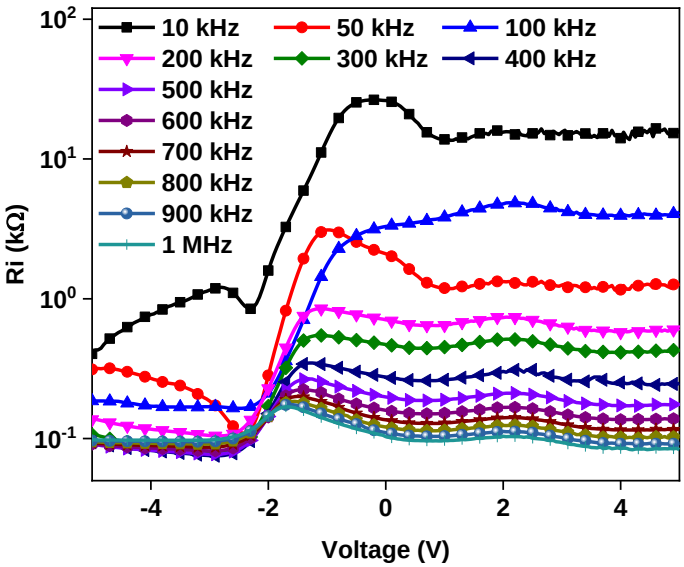

Figure 12. The R_i-V plots of the Au/CuNiCoS$_4$/*p*-Si photodiode for changing frequency

The photocurrent and photocapacitance behaviors of the Au/CuNiCoS$_4$/*p*-Si photodiode have been tested by the transient measurements with the on-off the light for various light intensity. While the photocurrent transient results have been exhibited in Fig. 13a, the photocapacitance transient graphs have been indicated in Fig. 13b for the increasing light power intensity. The photodiode has good response for on and off conditions of the light both photocurrent and photocapacitance values. The photocurrent and photocapacitance values increased with increasing light power intensity, but not linearly because they saturated towards higher light power after 60 mW.

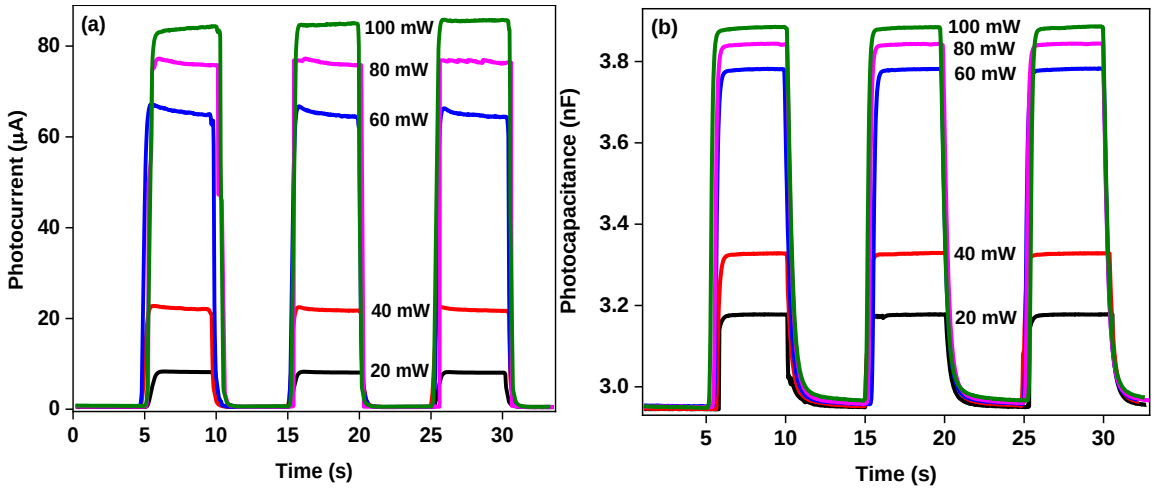

Figure 13. **a)** The photocurrent and **b)** photocapacitance changes of the Au/$CuNiCoS_4$/*p*-Si photodiode with various power illumination intensities

Conclusions

The $CuNiCoS_4$ nanocrystals were synthesized by hot-injection method successfully and tested as interfacial layer in a metal semiconductor heterostructure. The XRD pattern of the $CuNiCoS_4$ nanocrystals confirmed the crystal structure of the $CuNiCoS_4$ nanocrystals with the cubic phase Fd-3m (227) space group. The HR-TEM and FE-SEM images revealed that $CuNiCoS_4$ nanocrystals have spherical shape and 2.87 Å interplanar distances. The EDX analysis approved the composition of the $CuNiCoS_4$ nanocrystals and successfully synthesizing. The $CuNiCoS_4$ nanocrystals were inserted between the Au and *p*-Si to fabricate the Au/$CuNiCoS_4$/*p*-Si photodiode and characterized by *I-V* and *C-V* measurements for various light power intensities and frequencies, respectively. The ideality factor, barrier height, series and shunt resistance values as well as responsivity and specific detectivity were calculated and discussed in detail in terms of increasing light power. The Au/$CuNiCoS_4$/*p*-Si photodiode have 1.06 ideality factor and 0.81 eV barrier height values, but the ideality factor values increased and barrier height values decreased with increasing light

power. The device exhibited good rectifying behavior as well as good photodiode property at the reverse biases. The *C*-*V* characteristics of the Au/$CuNiCoS_4$/*p*-Si photodiode revealed that the capacitance values as well as other electrical parameters which extracted from C^{-2}-*V* plots strongly changed depending on the frequency and voltage. The results show that the fabricated Au/$CuNiCoS_4$/*p*-Si photodiode can be used in optoelectronic applications and has the potential to open new opportunities for improving the device performance.

Funding

This research is supported by Selçuk University BAP office with the research Project Number 17401159 and TUBITAK (The Scientific and Technological Research Council of Turkey) with project number 217M212.

References

(1) Tatarchuk, T.; Bououdina, M.; Judith Vijaya, J.; John Kennedy, L. *Springer Proc. Phys.* **2017**, *195*, 305–325. doi:10.1007/978-3-319-56422-7_22

(2) Hu, W.; Qin, N.; Wu, G.; Lin, Y.; Li, S.; Bao, D. *J. Am. Chem. Soc.* **2012**, *134* (36), 14658–14661. doi:10.1021/ja305681n

(3) Naumann, R. J. *Introduction to the Physics and Chemistry of Materials*; CRC Press, 2008. doi:10.5860/choice.46-6224

(4) Vaughan, D. J.; Burns, R. G.; Burns, V. M. *Geochim. Cosmochim. Acta* **1971**, *35* (4), 365–381. doi:10.1016/0016-7037(71)90079-2

(5) Wiltrout, A. M.; Read, C. G.; Spencer, E. M.; Schaak, R. E. *Inorg. Chem.* **2016**, *55* (1), 221–226. doi:10.1021/acs.inorgchem.5b02158

(6) Wen, T.; Zhang, Q.; Li, N.; Wang, Y.; Zhang, D.; Wang, L.; Yang, W. *Inorg.*

Chem. **2019**, *58* (19), 12628–12634. doi:10.1021/acs.inorgchem.9b01351

(7) Yıldırım, M.; Kocyigit, A.; Sarilmaz, A.; Ozel, S. S.; Kus, M.; Ozel, F. *J. Electron. Mater.* **2020**, *49* (2), 949–958. doi:10.1007/s11664-019-07841-z

(8) Sarilmaz, A.; Yanalak, G.; Aslan, E.; Akyildiz, H.; Patir, I. H.; Ozel, F. *Mater. Today Energy* **2020**, *16*, 100413. doi:10.1016/j.mtener.2020.100413

(9) Liu, D.; Lu, Q.; Luo, Y.; Sun, X.; Asiri, A. M. *Nanoscale* **2015**, *7* (37), 15122–15126. doi:10.1039/c5nr04064g

(10) Wu, X.; Li, S.; Liu, J.; Yu, M. *ACS Appl. Nano Mater.* **2019**, *2* (8), 4921–4932. doi:10.1021/acsanm.9b00891

(11) Mohammadi, A.; Moosavifard, S. E.; Goljanian Tabrizi, A.; Abdi, M. M.; Karimi, G. *ACS Appl. Energy Mater.* **2019**, *2* (1), 627–635. doi:10.1021/acsaem.8b01651

(12) Luo, Q.; Gu, Y.; Li, J.; Wang, N.; Lin, H. *J. Power Sources* **2016**, *312*, 93–100. doi:10.1016/j.jpowsour.2016.02.037

(13) Thompson, M. J. *Synthesis and Modification of Ternary and Quaternary Chalcogenide Nanocrystals*

(14) Gullu, H. H.; Yildiz, D. E.; Kocyigit, A.; Yıldırım, M. *J. Alloys Compd.* **2020**, *827*, 154279. doi:10.1016/j.jallcom.2020.154279

(15) Zhou, X.; Hu, X.; Jin, B.; Yu, J.; Liu, K.; Li, H.; Zhai, T. *Adv. Sci.* **2018**, *5* (8), 1800478. doi:10.1002/advs.201800478

(16) Fan, P.; Chettiar, U. K.; Cao, L.; Afshinmanesh, F.; Engheta, N.; Brongersma, M. L. *Nat. Photonics* **2012**, *6* (6), 380–385. doi:10.1038/nphoton.2012.108

(17) Kocyigit, A.; Yilmaz, M.; Aydogan, S.; Incekara, U.; Sahin, Y. *Polym. Test.* **2020**, *89*, 106546. doi:10.1016/j.polymertesting.2020.106546

(18) Cifci, O. S.; Bakir, M.; Meyer, J. L.; Kocyigit, A. *Mater. Sci. Semicond. Process.* **2018**, *74*, 175–182. doi:10.1016/J.MSSP.2017.10.039

(19) Yeap, S. P.; Lim, J.; Ooi, B. S.; Ahmad, A. L. *J. Nanoparticle Res.* **2017**, *19* (11), 368. doi:10.1007/s11051-017-4065-6

(20) Aslan, F.; Esen, H.; Yakuphanoglu, F. *Silicon* **2020**, *12* (9), 2149–2164. doi:10.1007/s12633-019-00306-2

(21) Gozeh, B. A.; Karabulut, A.; Yildiz, A.; Yakuphanoglu, F. *J. Alloys Compd.* **2018**, *732*, 16–24. doi:10.1016/j.jallcom.2017.10.167

(22) Cifci, O. S.; Kocyigit, A.; Sun, P. *Superlattices Microstruct.* **2018**, *120*, 492–500. doi:10.1016/J.SPMI.2018.06.009

(23) Karataş, Ş. *Microelectron. Eng.* **2010**, *87* (10), 1935–1940. doi:10.1016/j.mee.2009.11.168

(24) Erdal, M. O.; Kocyigit, A.; Yıldırım, M. *Mater. Sci. Semicond. Process.* **2019**, *103*, 104620. doi:10.1016/j.mssp.2019.104620

(25) Sze, S. M. *Physics of Semiconductor Devices*, 2. edition.; Wiley: Newyork, 1981

(26) Rao, L. D.; Reddy, V. R. *AIP Conf. Proc.* **2016**, *1731* (1), 120020. doi:10.1063/1.4948092

(27) Yilmaz, M.; Kocyigit, A.; Cirak, B. B.; Kacus, H.; Incekara, U.; Aydogan, S. *Mater. Sci. Semicond. Process.* **2020**, *113*, 105039. doi:10.1016/j.mssp.2020.105039

(28) Elamen, H.; Badali, Y.; Güneşer, M. T.; Altındal, Ş. *J. Mater. Sci. Mater. Electron.* **2020**, 1–9. doi:10.1007/s10854-020-04406-3

(29) Norde, H. *J. Appl. Phys.* **1979**, *50* (7), 5052–5053. doi:10.1063/1.325607

(30) Dayan, O.; Gencer Imer, A.; Al-Sehemi, A. G.; Özdemir, N.; Dere, A.; Şerbetçi, Z.; Al-Ghamdi, A. A.; Yakuphanoglu, F. *J. Mol. Struct.* **2020**, *1200*, 127062. doi:10.1016/j.molstruc.2019.127062

(31) Mekki, A.; Dere, A.; Mensah-Darkwa, K.; Al-Ghamdi, A.; Gupta, R. K.; Harrabi, K.; Farooq, W. A.; El-Tantawy, F.; Yakuphanoglu, F. *Synth. Met.* **2016**, *217*, 43–56. doi:10.1016/j.synthmet.2016.03.015

(32) Tataroğlu, A.; Altındal; Azizian-Kalandaragh, Y. *Phys. B Condens. Matter* **2020**, *582*, 411996. doi:10.1016/j.physb.2020.411996

(33) Nezhadesm-Kohardafchahi, S.; Farjami-Shayesteh, S.; Badali, Y.; Altındal; Jamshidi-Ghozlu, M. A.; Azizian-Kalandaragh, Y. *Mater. Sci. Semicond. Process.* **2018**, *86*, 173–180. doi:10.1016/j.mssp.2018.06.030

(34) Türüt, A. *Turkish J. Phys.* **2020**, *44* (4), 302–347

(35) Erdal, M. O.; Kocyigit, A.; Yıldırım, M. *Chinese J. Phys.* **2020**, *64*, 163–173. doi:10.1016/j.cjph.2019.12.021

(36) Al Orainy, R. H.; Hendi, A. A. *Microelectron. Eng.* **2014**, *127*, 14–20. doi:10.1016/j.mee.2014.02.014

(37) Yıldırım, M.; Kocyigit, A. *J. Alloys Compd.* **2018**, *768*, 1064–1075. doi:10.1016/j.jallcom.2018.07.295

(38) Kocyigit, A.; Yılmaz, M.; Aydoğan, Ş.; İncekara, Ü. *J. Alloys Compd.* **2019**, *790*, 388–396. doi:10.1016/j.jallcom.2019.03.179

(39) Sevgili, Ö.; Azizian-Kalandaragh, Y.; Altındal, Ş. *Phys. B Condens. Matter* **2020**, *587*, 412122. doi:10.1016/j.physb.2020.412122

(40) Erdal, M. O.; Kocyigit, A.; Yıldırım, M. *Microelectron. Reliab.* **2020**, *106*, 113591. doi:10.1016/j.microrel.2020.113591

(41) Baraz, N.; Yücedağ, İ.; Azizian-Kalandaragh, Y.; Altındal, Ş. *J. Mater. Sci. Mater. Electron.* **2017**, *28* (2), 1315–1321. doi:10.1007/s10854-016-5662-3